A phenomenological cluster-based model of Ca^{2+} waves and oscillations for Inositol 1,4,5-trisphosphate receptor (IP_3R) channels

Svitlana Braichenko* and Atul Bhaskar

Faculty of Engineering and the Environment,

University of Southampton, SO17 1BJ, Southampton, UK

Srinandan Dasmahapatra

School of Electronics and Computer Science,

University of Southampton, SO17 1BJ, Southampton, UK

(Dated: August 24, 2018)

Abstract

Clusters of IP_3 receptor channels in the membranes of the endoplasmic reticulum (ER) of many non-excitable cells release calcium ions in a cooperative manner giving rise to dynamical patterns such as Ca^{2+} puffs, waves, and oscillations that occur on multiple spatial and temporal scales. We introduce a minimal yet descriptive reaction-diffusion model of IP_3 receptors for a saturating concentration of IP_3 using a principled reduction of a detailed Markov chain description of individual channels. A dynamical systems analysis reveals the possibility of excitable, bistable and oscillatory dynamics of this model that correspond to three types of observed patterns of calcium release – puffs, waves, and oscillations respectively. We explain the emergence of these patterns via a bifurcation analysis of a coupled two-cluster model, compute the phase diagram and quantify the speed of the waves and period of oscillations in terms of system parameters. We connect the termination of large-scale Ca^{2+} release events to IP_3 unbinding or stochasticity.

PACS numbers: 82.20.Wt, 82.40.Bj, 82.40.Ck

---

* Corresponding author; braichenko.svitlana@gmail.com

I. INTRODUCTION

Ionic calcium (Ca^{2+}) is a second messenger involved in many processes such as fertilization, cell proliferation, differentiation, embryonic development, secretion, muscular contraction, immune response, brain functions, chemical sensing, light transduction, etc. [1, 2]. While many types of Ca^{2+} release channels are implicated in these processes, in this paper we are concerned with the dynamics of Ca^{2+} released into the cytosol from inositol 1,4,5-triphosphate receptor (IP_3R) channels [2] that are triggered by IP_3 secondary messenger molecules. IP_3R channels are usually present in non-excitable cells and are mainly localized in the endoplasmic reticulum (ER) membrane where they are believed to form tight clusters to enable Ca^{2+} signaling. Experimental observations [3, 4] suggest that the distribution of clusters varies by cell type. For example, SH-SY5Y neuroblastoma cells contain around 4 to 6 channels per cluster (a few contain up to 10 channels), HeLa cells clusters on average contain 2 to 3 channels and *Xenopus* oocytes clusters contain around 20 channels each [5]. However, theoretical and experimental investigations of clustering and the mechanisms by which it regulates Ca^{2+} signaling are incomplete and is the subject of ongoing research.

Ca^{2+} signaling events corresponding to release from Ca^{2+} channels [1] constitute a multiscale hierarchy consisting of three distinct types of events taking place at different spatial and temporal scales involving individual channels, clusters of channels and groups of channel clusters. The events occurring at the smallest scale ($\sim 10\,\text{nm}$ and $\sim 10\,\text{ms}$) are called *blips*. They are the building blocks of signals on larger scales. Blips occur when Ca^{2+} is released from a single channel into the cytosol. Coordinated Ca^{2+} release from a cluster of channels – a collection of co-occurring blips – is called a puff and appears at the second level of the hierarchy ($\sim 100\,\text{nm}$ and $\sim 100\,\text{ms}$). This cooperation between signaling events is regulated by Ca^{2+} in a concentration-dependent feedback mechanism. Low Ca^{2+} concentrations (maximum activity for $200 - 500$ nM) diffuse around the cytosol and cause further release from neighboring channels, whereas Ca^{2+} in high cytosolic concentrations inhibits further Ca^{2+} release. This feedback mechanism is called Ca^{2+} induced Ca^{2+} release (CICR). The final level in the hierarchy ($\sim 1\,\mu\text{m}$ and $\sim 1\,\text{s}$) is associated with Ca^{2+} *spikes*, *waves*, and *oscillations*. Spikes correspond to local or global transient releases from a group of clusters. Ca^{2+} waves are formed as sequential releases travel from excited clusters to neighboring ones. Ca^{2+} oscillations are repetitive Ca^{2+} spikes or waves. All the events on the highest

2

hierarchical level that we consider (spikes, waves, oscillations) consist of the coordinated release of Ca^{2+} puffs from a group of clusters.

Ca^{2+} oscillations are experimentally observed in various types of cells [6]. Many models associate the occurrence of Ca^{2+} oscillations with the IP_3 regulation [6–10]. Some studies connect the emergence of Ca^{2+} oscillations with the oscillating level of IP_3 triggered by binding to various enzymes, such as PLC (phospholipase C) or IP_3 kinase [6, 9]. Others report that Ca^{2+} oscillations may occur even if the IP_3 concentration is non-oscillatory [7, 8]. Various studies explain oscillatory Ca^{2+} behavior as a sequence of stochastic spikes [11–13]. Apart from oscillations and spikes propagating wavefronts have also been much studied. These are implicated, for instance, in oocyte fertilization, and are generated when a sperm cell makes contact with an oocyte.

There is an extensive literature on the deterministic modeling of Ca^{2+} front propagation. References [7, 8, 14–17] consider the averaged Ca^{2+} dynamics from a well-mixed ER membrane without addressing the clustering of channels. Channel clusters, including inhomogeneous cluster distributions [18], are considered in deterministic [19–21] and stochastic models [19, 22] of Ca^{2+} wave propagation. The current paper studies the deterministic properties of Ca^{2+} waves and oscillations occurring in the ER membrane containing multiple clustered channels. The models in [20, 21] inject a burst of Ca^{2+} ions at each cluster which diffuses between clusters. While the burst size is represented by a parameter in their models, we choose to represent the release mechanism by a reduced version of the DYK [7] model proposed by Rüdiger [23]. This gives our model access to single channel characteristics [7] and cluster properties [23] providing more mechanistic insight into the link between single-channel properties and features of waves and oscillations at higher levels in the spatial hierarchy. We use dynamical systems analysis to explore the different dynamical regimes at the single-cluster level and relate these properties to larger spatial scales. Thus, unlike the fire-diffuse-fire model [20, 21] we can study the characteristics of global Ca^{2+} release events such as waves and oscillations, including their inhibition and termination, using channel and cluster parameters. We also build on the results of a detailed hybrid stochastic-deterministic single-cluster study [24] and its extension on a grid of clusters [25] that show different durations of Ca^{2+} events depending on the IP_3 level.

In detail, we introduce a spatial model of Ca^{2+} waves and oscillations building upon qualitative insights from dynamical systems theory applied to reduced, few variable mod-

els [8, 23] of IP$_3$R channel subunits [7] integrated into channels and heterogeneous clusters of channels [24]. We assume the IP$_3$ concentration to be sustained at a high level so that it increases the probability of the occurrence of Ca^{2+} waves and oscillations, extending the observation of excitability of channel clusters in [23]. Further, we account for variability of [IP$_3$] levels by including the IP$_3$ unbinding. The extended model also gives insight on the numbers of activatable channels (all four subunits has IP$_3$ bound [26]) in agreement with [24, 25]. The model we propose is of a deterministic reaction-diffusion type where diffusion of Ca^{2+} between clusters of channels smooths the Ca^{2+} releases from individual activated clusters modeled by reaction dynamics. Here we study the dependence of the velocity and period of waves and oscillations on the diffusion coefficient, equilibration rate and a number of channels in each cluster. We observe a curious spatially alternating wave pattern in a regime of parameter space that is reminiscent of the occurrence of intracellular spatially organized Ca^{2+} alternans [27]. The termination of large-scale events such as waves and oscillations has been a topic of considerable discussion [28–32]. We provide evidence for two different mechanisms – a stochastic termination and a deterministic IP$_3$ unbinding – that can be accommodated in our models in order to account for the decay of Ca^{2+} excitations in simulation traces.

II.   METHODS

A kinetic model of channel activation and deactivation is the basis for models of Ca^{2+} dynamics, and many models [8, 23] have been proposed that reduce the detailed kinetic scheme laid out by De Young and Keizer – the so-called DYK model [7] as a starting point. Our approach to simplifying the complexity of the problem is based on several basic models briefly discussed in this section. The assumption of a well-mixed membrane where spatial effects are ignored is a shared limitation of these models [7, 8]. The spatial extension of the three-state model [23] is proposed in the last subsection. For further details please refer to the Appendices and Supporting Material.

A. DYK and derived models of Ca^{2+} signaling

The DYK model [7] is one of the first models which successfully accounts for key empirical findings of IP_3R channels. In the model each channel consists of four subunits, at least three of which need to be activated for channel opening, reflecting the three conductance levels experimentally observed in [33]. Each subunit has 3 binary state variables $i, j, k \in \{0, 1\}$, corresponding to 3 binding sites – for IP_3, activating Ca^{2+} and inhibiting Ca^{2+} – with a state transition diagram shown in Fig. 1 (a) and described in its caption. The fraction of subunits in a given state (ijk) is represented by the variable x_{ijk}, such that they sum up to unity, i.e. $\sum_{i=0}^{1} \sum_{j=0}^{1} \sum_{k=0}^{1} x_{i,j,k} = 1$. The presence of IP_3 at each channel enhances Ca^{2+} release, while calcium either amplifies or inhibits further Ca^{2+} release (called calcium-induced calcium release, CICR).

The DYK model assumes that all 4-subunit channels are "well-mixed" in the membrane and dispenses with spatial effects such as clustering. The complexity of the state space of the model makes it computationally difficult to obtain properties of the spatial distribution of channel clusters in the ER membrane. Hence, multiple attempts at reducing its complexity have been made in the last few decades, the majority of which share the common feature of IP_3-dependent activation and CICR.

In one such reduced model [8], the variables corresponding to the DYK cube [Fig. 1 (a)] are dispensed with by assuming that activation by IP_3 and Ca^{2+} are fast, compared with the slow inhibition by Ca^{2+}. The state indices $(i, j, 0)$ and $(i, j, 1)$ distinguish the two states of the site where the inhibiting Ca^{2+} binds. The fractions x_{ij0} and x_{ij1} of states with variable IP_3 and activating Ca^{2+} binding sites on the left and the right faces of the DYK cube [Fig. 1 (a)] are slow variables in the slow-fast reduction. The pairs of fractions (x_{0j0}, x_{1j0}) and (x_{0j1}, x_{1j1}) are determined from the steady state of the fast IP_3 binding and unbinding processes. The dynamics of the reduced model is governed by the compound dynamics of the left-right faces and Ca^{2+}.

B. Single-cluster models

Another reduction of the dynamics of a group of DYK subunits is introduced in [23] where, in contrast to [8], dynamical variables capture the collective behavior of a cluster of
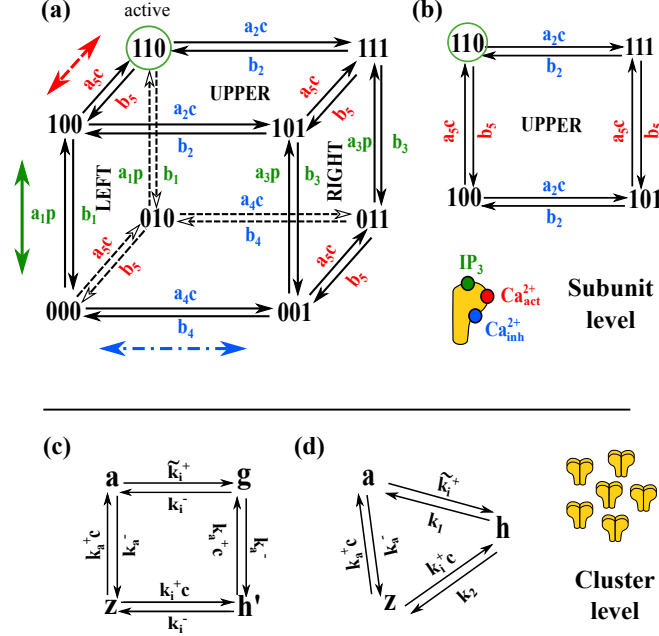
FIG. 1: (Color online) **(a) DYK cube.** Schematic diagram of the DYK eight-state gating model of the activation of a single subunit of an IP_3R channel; the eight corners of the schematic will be referred as the DYK cube [7]. Each vertex of the cube directly corresponds to a specific state of a subunit labeled with numbers ijk, where i corresponds to the IP_3 activating site, j to the Ca^{2+} activating site and k to the Ca^{2+} inhibiting site. Each binding site can be either unbound $(i, j, k = 0)$, or bound $(i, j, k = 1)$. The *green arrow* indicates binding (unbinding) of IP_3 to the binding site while *red dashed* and *blue dot-dashed arrows* correspond to Ca^{2+} activating and inhibiting transitions respectively. The transitions between the states are governed by the second-order ($a_l p$ or $a_l c$, where $p = [IP_3]$, $c = [Ca^{2+}]$), and the first-order (b_l) rate constants, where $l = \overline{1,5}$. **(b) Upper DYK plane.** When p is high, the most of the transitions take place in the upper plane of the cube. **(c) Four-state model.** The scheme of the model [23] for high p at the level of a cluster of channels. The fractions of the states in a cluster are marked as a, g, z, h' instead of $110, 111, 100, 101$ for subunits. The transition rates between channel states are $k_{a,i}^{\pm}$ and $\tilde{k}_i^+ = k_i^+ c_s$ to indicate the elimination of detailed balance in a cluster of channels [34]. **(d) Three-state model.** The final model includes a compound state h formed from the states g and h' with the effective rates $k_{1,2}$.

IP_3R channels. This model shows that for large values of IP_3 the dynamics is excitable, and explains the occurrence of Ca^{2+} puffs. As this model is the starting point of our analysis we

present the reduction of the IP$_3$ dynamics explicitly in Appendix A for completeness. Here we discuss its fundamental assumptions. The reduction scheme follows a similar slow-fast approach [8] but for the case of high $p = [\text{IP}_3]$. This assumption leads to fast transitions with rates $a_{1,3}p$ [Fig. 1 (a)] and all channel subunits are forced to have the IP$_3$ binding site occupied leaving only $1jk$ states to be dynamical (the upper plane of the DYK cube in Fig. 1 (a)). The dynamical variables of the four subunits shown in Fig. 1 (b) are gathered together to introduce cluster variables a, g, h', and z. These represent the fractions of channels within a cluster in the corresponding states shown in Fig. 1 (c). The transition rates k_a^-, $k_i^\pm$ are derived from the parameters in the DYK model [7]. The transition rate k_a^+ is obtained from the requirement that at least three subunits need to be activated to open a channel (A28). The numerical values of the coefficients [23] are provided in Table I. A further simplification – corresponding to the passage from Fig. 1 (c) to (d) – is introduced [23] by replacing the pair of states (g, h') representing IP$_3$ -bound, inactivating Ca^{2+} -bound states with a compound state h whose kinetics has effective rates k_1 and k_2 [(A32), (A33)]. This reduces the cluster dynamics to a two-state model as the subunit fractions within a cluster sum to unity, $z = 1 - a - g - h' = 1 - a - h$. A significant modeling assumption is made whereby the rates $\widetilde{k}_i^+$ and $k_i^+ c$ in Fig. 1 (c) are taken to be different [34], in contrast to the equal rates $a_2 c$ on the upper plane of Fig. 1 (a) made in [7], a condition that implies detailed balance.

The three-state model of a cluster of IP$_3$ channels thus obtained exhibits excitable and bistable dynamical regimes [23]. In our study, we modify the model slightly, by setting the parameters for a single cluster of channels to fit the open probability distribution of IP$_3$ channels in the presence of Ca^{2+} in *Xenopus* oocytes [24]. This leads to changes in the transition rates a_2 and b_2 as shown in Tab. I. Consequently, an oscillatory regime emerges in addition to the excitable and bistable regimes found in [23]. Later in this paper, we spatially extend this model in a cluster-based manner to study the interplay between the different regimes of clusters in producing wave and oscillation dynamics in a membrane.

The dynamics of a cluster is governed by the set of dynamical variables $x(t) = \{a(t), h(t), c(t)\}$ corresponding to the fraction in the cluster of opened channels $a(t)$, inhibited channels $h(t)$, and the cytosolic Ca^{2+} concentration $c(t)$. The dynamical variables in the phase space, as shown in Fig. 1 (d), are governed by a system of coupled ordinary differential equations [23]

TABLE I: Parameters used in the model in [23] and the single cluster model of this paper.

Parameter	Rüdiger [23]	Present study
Ca^{2+} activation binding rate a_5, $\mu M^{-1} \times s^{-1}$	100	100
Ca^{2+} activation unbinding rate $(b_5, k_a^-)^a$, s^{-1}	20	20
Ca^{2+} inhibition binding rate $(a_2, k_i^+)^a$, $\mu M^{-1} \times s^{-1}$	0.1	0.02^a
Ca^{2+} inhibition unbinding rate $(b_2, k_i^-)^a$, s^{-1}	1.7	1.56^b
Local $[Ca^{2+}]$ at opened channel $\tilde{k}_i^+ = k_i^+ c_s$, s^{-1}	30	6^b
Rest level of $[Ca^{2+}]$ c_0, μM	0.025	$0.025 - 0.6$
Channel coupling constant α, μM	0.74	0.74
Number of activatable channels N	9 or 25	5 or 6
Equilibration rate λ, s^{-1}	10^3	10^3
Characteristic of the step ϵ	0.1	0.1

[a] Here we show the transition rates for subunit and channel as shown in Figs. 1 (b) and (c) respectively. These rates are assumed to be the same in this study.

[b] These values are determined from patch-clamp data on the probability distribution for channel opening typical for *Xenopus* oocytes at high $[IP_3]$ [24]

$\dot{x} = F(x(t))$ with appropriate initial conditions:

$$\frac{\mathrm{d}a}{\mathrm{d}t} = k_a^+(c)c(1 - a - h) - k_a^- a + k_1(c)h - \tilde{k}_i^+ a$$
$$\triangleq f(a, h, c), \tag{1}$$
$$\frac{\mathrm{d}h}{\mathrm{d}t} = k_i^+ c(1 - a - h) - k_1(c)h - k_2(c)h + \tilde{k}_i^+ a$$
$$\triangleq g(a, h, c). \tag{2}$$

The rates $k_a(c)$, $k_1(c)$ and $k_2(c)$ are given in eqs. (A28), (A32) and (A33), respectively [23, 32]. It is assumed in [34] that after a blip Ca^{2+} levels at a channel pore remain high while neighboring channels in a cluster relax to levels around c_d. According to [35] $[Ca^{2+}]$ at a nanodomain drops rapidly from several hundreds of μM to a few μM. Thus, at the timescales of the dynamics studied in [23] and in our paper, the calcium-dependent inactivation rate is taken to be frozen at $\tilde{k}_i^+ = k_i^+ c_s$ as shown in the transition scheme Fig. 1 (c), (d). The dynamics of the c variable accounts for homeostatic mechanisms such as pumps and buffers in the simplest way, whereby Ca^{2+} levels relax back to a steady-state level $c_d(a)$ at rate λ:

$$\frac{\mathrm{d}c}{\mathrm{d}t} = -\lambda[c - c_d(a)], \tag{3}$$

where $\lambda = 10^3 \, \mathrm{s}^{-1}$ [23] sets the fast time-scale so that $c_d(a)$ is slaved to the dynamics of $a(t)$. The activation barrier for a cluster of channels is modeled separately by setting a threshold below which the cytosolic level of calcium is c_0 and above which the concentration of Ca^{2+} is approximately linear in the number of opened channels Na:

$$c_d(a) = c_0 + 0.5\alpha Na \left\{1 + \tanh[(Na - 1)/\epsilon]\right\}, \tag{4}$$

where ϵ sets the scale for smoothing the transition from zeroth to first order dependence on opening and α is a constant defining the strength of the coupling between channels in a cluster. Such a step is proposed in [23] to avoid Ca^{2+} release from the inactive clusters where the number of opened channels $Na < 1$. This modeling step is necessary because a and h denoting fractions of opened or inhibited channels are continuous variables.

The assumption of fast equilibration to steady-state level c_d in (3) flattens out $c(t)$ from its blip amplitude c_s of cytosolic Ca^{2+} at a cluster. For $\lambda = 10^3 \, \mathrm{s}^{-1}$ [23], it takes $\sim 1 - 10$ ms for Ca^{2+} levels to reach cytosolic concentrations in the $10 - 10^3$ nM range. In what follows, we introduce a diffusion term to enable Ca^{2+} to activate quiescent clusters by CICR
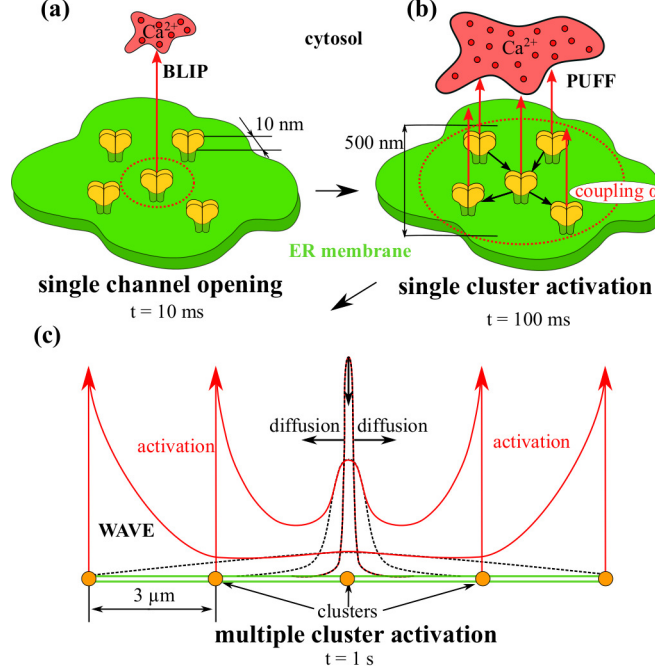
9

FIG. 2: (Color online) Schematic representation of the spatial and temporal hierarchy of Ca^{2+} release events. **(a)** A blip as the release from a single channel. The *green plane* represents a part of the ER membrane, the *red arrow* indicates Ca^{2+} release from the opened channel indicated by the *dotted circle*. **(b)** A puff is represented by multiple blips occurring in a single cluster of coupled channels. The coupling between channels (marked by *black arrows*) is defined by the constant α in the nonlinear dependence (4). **(c)** The wave propagation as a sequence of puffs (*red lines*) caused by raised levels of $[Ca^{2+}]$. In our modeling approach, we consider clusters of channels to be localized at single points in space. The activation of neighboring clusters is caused by Ca^{2+} diffusion from the initial Ca^{2+} release localized in the center (*black dotted lines*).

thereby having blips combine to form puffs as shown in Fig. 2 (b). This is reminiscent of the fire-diffuse-fire model [21].

For a single cluster in a small domain of the membrane a computational study [24] using a hybrid reaction-diffusion model – a Markov chain description as per DYK [7] and partial differential equations for diffusing Ca^{2+} ions – shows the dependence of the transition from puffs to waves on the numbers of channels in a cluster which initiate Ca^{2+} release events under different IP_3 loads. The complexity of the analysis prompts us to look for a simplified model that could probe the temporal patterns observed and provide qualitative explanations

10

for their origin via dynamical systems theory. We extend this study to a larger domain containing multiple clusters each described by (1)–(2) [23]. While retaining the structure of the model given in [23] we chose the parameters of [24] in order to study the effect of different numbers of channels in each cluster and the interplay between them. This allows us not only to study the transition from puffs to waves but to obtain the characteristics of waves and oscillations that emerge.

This is the justification of applying the principles of slow-fast reduction to the single channel and single cluster models – we can elucidate how these reduced models may be coupled to account for physiological behavior that is manifest spatially.

C.   Cluster-based spatial model

In this section, we lay down our assumptions for building a spatially dependent model for a phenomenological representation of a Ca^{2+} wave as a set of sequential Ca^{2+} release from clusters [Fig. 2 (c)] using features of earlier models [7, 8, 15, 21, 23, 24]. An examination of the dynamical regimes of individual cluster-level reductions that account for the blip to puff phenomena enables us to propose a model of diffusively coupled clusters in the ER membrane where Ca^{2+} release occurs. We analyze the clusters separately using dynamical systems theory. We confirm the existence of two qualitatively different Ca^{2+} behaviors in clusters with different numbers of channels, *viz.*, excitable (puff regime) and bistable (wave regime) [23]. We shall probe whether introducing diffusive coupling and linear relaxation (3) (that can subsume effects including buffering [16] or other modes of reducing spatial gradients) can facilitate the occurrence of oscillations in Ca^{2+} release in the ER membrane. This is incorporated into the model by modifying the equilibration eq. (3) by introducing a one-dimensional diffusive transport term

$$\frac{\partial c}{\partial t} = D\frac{\partial^2 c}{\partial x^2} - \lambda \sum_i H(r_{cl} - |x - x_i|)\left(c - c_d(a_i)\right),\tag{5}$$

where $c_d(a_i)$ is given by eq. (4), D is an effective diffusion constant, x is a spatial coordinate, $H(x)$ is the Heaviside step-function ensuring that calcium releases into the cytoplasm occur only at the clusters located at x_i, $i = \overline{1, L}$, and r_{cl} is the cluster radius.

$$H(x) = \begin{cases} 1, & \text{if } x \geq 0, \\ 0, & \text{otherwise.} \end{cases}\tag{6}$$

For the convenience of notation, we shall assume that the i dependence on a_i is implicit hereafter.

The model proposed in the current paper is of the fire-diffuse-fire type studied before [21]. Unlike previous studies, we propose a direct link between the Ca^{2+} level c and the proportion of opened channels a through nonlinear eq. (4). This also helps us to associate cellular behavior of Ca^{2+} releases on a spatial scale larger than the cluster size r_{cl} to microscopic channel characteristics [7].

System (1)–(2) together with eq. (5) is a reaction-diffusion system. The first term in the eq. (5) corresponds to the smoothing of a Ca^{2+} front and the spreading of $[Ca^{2+}]$ from the active clusters to the neighboring ones as sketched in Fig. 2 (c). In the second, reaction term, c_d (4) is a function of the number of opened channels and accounts for the opening of IP_3R channels in the clusters. The equilibration of cytosolic Ca^{2+} to c_d at rate λ is a linear homeostatic reaction term that subsumes the action of pumps, leaks, and buffers, which drives the cytosolic $[Ca^{2+}]$ to the steady state value c_d.

We explore next how this model is able to generate waves and oscillations and characterize these phenomena in terms of the model parameters.

III. RESULTS

In subsection III A, we apply the three-state model to a case of high $[IP_3]$ and corroborate the existence of a transition from excitable to bistable behavior in a cluster of channels [23]. By continuously changing the rest Ca^{2+} concentration parameter c_0 in a cluster with no opened channels, we uncover the existence of two Hopf bifurcations. This illustrates the possibility that a single cluster could exhibit oscillations and channel activity and homeostatic mechanisms could regulate the state of the system to undergo dynamical regime shifts.

Instead of letting c_0 be a fixed external control parameter that sets the level of Ca^{2+} ions in the appropriate range for oscillatory behavior in the bifurcation analysis, we allow Ca^{2+} levels to be dynamically set by diffusion, with the effective diffusion constant D being the control parameter that sets the Ca^{2+} levels locally and affecting the physiological output. Diffusion levels gradients; in order to ascertain whether altering the levels between a cluster primed for bistability and that which is excitably monostable, we set up in subsection III B a

12

two-cluster model to study its phase diagram by bifurcation analysis. Once again, we find the existence of two Hopf bifurcation points as D is altered and obtain the corresponding limit cycle trajectories. We associate those trajectories with the emergence of Ca^{2+} oscillations.

In the subsection III C, we apply our cluster-based model to study Ca^{2+} release from a domain in the ER membrane with clusters containing different numbers of channels. We demonstrate how the interplay between excitable and bistable clusters is a mechanism for the emergence of Ca^{2+} oscillations within the ER membrane. We also show that the cluster-based model is capable of exhibiting Ca^{2+} waves that propagate throughout the membrane.

In the subsection III D, we show the role of the IP_3 unbinding in the termination of the Ca^{2+} release from a bistable cluster. We account for the transitions between the upper and lower planes of the DYK cube for varying $[IP_3]$ levels.

A. Ca^{2+} dynamics at the scale of a single cluster

We study the three-state model in eqs. (1), (2) with parameters as shown in the last column of Table I. We shall treat as control parameters for our bifurcation analysis N, the number of channels in a cluster and c_0, the rest concentration of Ca^{2+} ions when none of the channels are opened, with $(0.025 \leq c_0 \leq 0.6)\,\mu M$. The choice of transition rates $k_i^+ = 0.02\,(\mu M \cdot s)^{-1}$ and $k_i^- = 1.56\,s^{-1}$ were determined by patch-clamp data on the probability distribution for channel opening typical for *Xenopus* oocytes at high $[IP_3]$ [24]. This has implications on the number of channels to be opened within each cluster in shaping the model building and results below.

We assume that cytosolic $[Ca^{2+}]$ equilibrates to the steady-state value c_d very fast ($\lambda = 10^3\,s^{-1}$) in eq. (3). Therefore, we are able to represent the model of a single cluster dynamics by eqs. (1), (2) whose solutions are numerically obtained by standard Runge-Kutta methods and shown in the (a, h) phase plane in Figs. 3 (a), (b), and (c). In the next subsections, this value will be reduced and the corresponding fast-slow decoupling will no longer be valid.

Figs. 3 (a) and (b) show system behavior as determined by the orientation and position of the $\dot{a} = f(a, h) = 0$ (*green dashed line*) and $\dot{h} = g(a, h) = 0$ (*red solid line*) nullclines and we mark by 'X' the locations of the stable fixed points where the nullclines intersect. The *broken arrow* represents a perturbation of the system away from the stable fixed point closest to the origin. After excitation, the system evolves following the trajectory which is
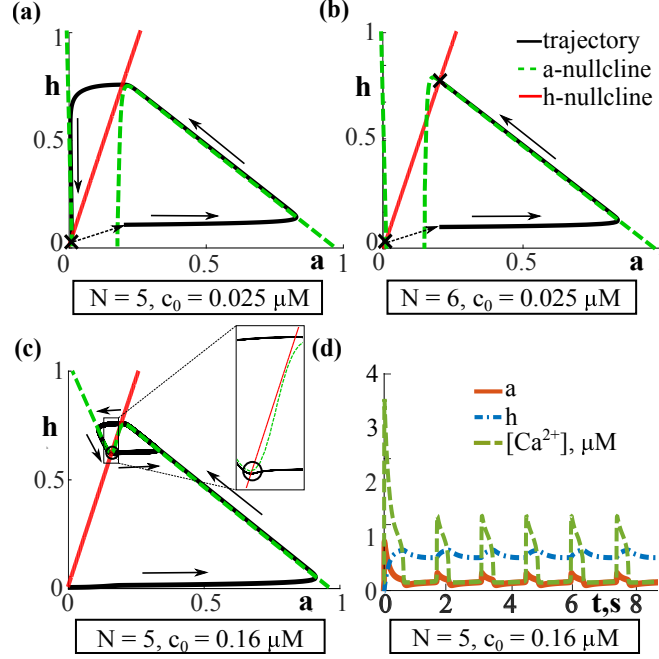
13

FIG. 3: (Color online) The different regimes of Ca^{2+} release in the two-dimensional three-state model (1)–(2) assuming $c = c_d$ given by (4) [23]. **(a)** The phase diagram of the excitable cluster ($N = 5$), the *red solid line* is h-nullcline for inhibition, the *green dashed line* is a-nullcline for opened channel with at least three active Ca^{2+} bound, the *black solid line* is a trajectory started from $a = 0.2$, $h = 0.1$ (*black arrows*) and finished at the stable fixed point (*black cross*). **(b)** The phase diagram of the bistable cluster ($N = 6$), the diagram depicts two stable fixed points. The trajectory starts at $a = 0.2$, $h = 0.1$ and finishes at the upper fixed point. **(c)** Oscillations in the three-state model observed for $N = 5$ and $c_0 = 0.16 \, \mu M$. The only unstable fixed point is marked as the *open circle* in the zoomed figure. **(d)** The temporal behavior of oscillations for a fraction of channels in open state denoted a *(red solid)*, a fraction of closed channels denoted h *(blue dot-dashed)*, and cytosolic $[Ca^{2+}]$ denoted c *(green dashed)*.

guided by the nullclines (*green dashed* and *red solid lines*). If the initial condition for the dynamical variables in Fig. 3 (a) lies to the right of the middle *green dashed line*, the state variables return to the (only) fixed point following the extended trajectory in the phase plane shown in *black*. In Fig. 3 (a) the trajectory comes back to the only fixed point and demonstrates that the monostable state is an excitable one, while in Fig. 3 (b) the system settles into the fixed point corresponding to the higher values of (a, h), a bistable state. The

excitable dynamics creates a short-lasting puff when the Ca^{2+} concentration is pulse-like. In contrast, the bistable cluster dynamics ensures that the Ca^{2+} concentration does not return to a base level but stays elevated for a longer period of time, the behavior associated with a long-lasting puff. The termination of such a long-lasting puff is attributed to IP_3 unbinding which is discussed in subsection III D. Also, we shall show later the possible role of the intra-cluster, inter-channel coupling represented by α in eq. (4) in accounting for termination of puffs.

We confirm the transition from monostable excitable and bistable behavior [23] in Figs. 3 (a) and (b). However, our use of parameters adapted from [24] reveals the bistable state occurs when the number of channels is $N \geq 6$ unlike the higher value $N \geq 9$ in [23]. $N \sim 5, 6$ was an average number of open channels when calcium waves were triggered as a function of increasing IP_3 the hybrid reaction-diffusion simulation [24]. Having confirmed that changing the total number of channels that may be opened alters the dynamics, we then analyze the stability of the lower fixed point in the phase plane upon changes of parameter c_0. As seen in Figs. 3 (a) and (b), the rest concentration of Ca^{2+} ions is taken as $c_0 = 0.025 \, \mu M$. We change c_0 in a continuous manner $(0.025 \leq c_0 \leq 0.6) \, \mu M$ to probe qualitative shifts in system dynamics. The bifurcation diagram is shown in Fig. 4 (a) and the real and imaginary parts of the eigenvalues $(\lambda_{1,2})$ of the Jacobian of the system in Figs. 4 (c) and (d). We find two Hopf bifurcation points $(\Re(\lambda_1, \lambda_2) = 0$ and $\Im(\lambda_1, \lambda_2) \neq 0)$ in the range of c_0 that determine the onset or disappearance of limit cycles.

c_0 is an external control parameter in the bifurcation analysis with values in a physiologically plausible range. It is the cytosolic $[Ca^{2+}]$ at a cluster before a Ca^{2+} release event commences when no channels are opened. The oscillatory behavior of the dynamical variables of the cluster with initial condition $c_0 = 0.16 \, \mu M$ for the concentration of Ca^{2+} is shown in Figs. 3 (c) and (d) in two different representations.

To study the stability of the limit cycles emerging from the Hopf bifurcation we perform a detailed dynamical systems analysis, presenting the results of the continuation and bifurcation analysis performed using the MatCont [36] package for Matlab in Fig. 4. This analysis keeps track of how a continuous change in parameters such as c_0 alters the fixed point shown in Fig. 3 (a) and, thus, the eigenvalues of the Jacobian around the altered fixed point change as well (see, e.g., Fig. 3 (c)). In particular, we calculate the first Lyapunov coefficient l_1 (see [37]) derived from the normal form of the system of eqs. (1), (2), at each
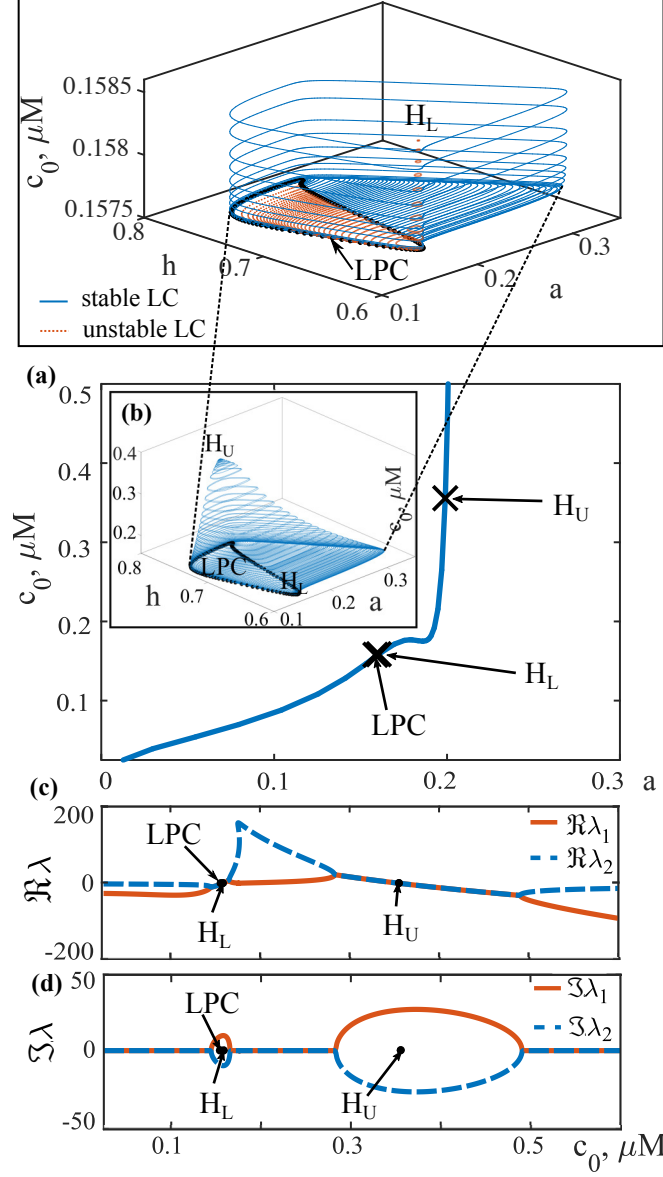
FIG. 4: (Color online) **(a)** Bifurcation diagram of the two-dimensional system at $N = 5$ plotted versus control parameter c_0, *black crosses* labeled by H_L and H_U correspond to Hopf bifurcation points ($\Re\lambda = 0$, $\Im\lambda \neq 0$), LPC corresponds to the value of c_0 where the fold bifurcation of two limit cycles occurs. **(b)** The stable limit cycle emerges at a supercritical Hopf point labeled as H_U. The continuation of the stable limit cycle shown by *blue solid lines*. With the decrease in c_0 the unstable limit cycle occurs from subcritical H_L point as indicated by *red dashed lines* of small amplitude in zoomed view. *Black dotted*

(continued)

16

FIG. 4: *line* corresponds to the fold (limit point) bifurcation of two limit cycles marked as LPC. **(c)** The real parts of the first two eigenvalues of the system, which are zeros at Hopf points. **(d)** The imaginary parts of the eigenvalues of the system are non-zeros at Hopf points. Two saddle-node bifurcation points are also present in the diagram at $c_0 \approx 0.18 \, \mu$M, however, we do not show them in the plot as these points are not relevant to the analysis below and will no longer be discussed.

Hopf point (denoted H_U and H_L), assuming $c = c_d$ as in eq. (4). If l_1 is positive (negative) the Hopf bifurcation is subcritical (supercritical) and the limit cycle is unstable (stable). In our case, $l_1 = -2.9 \times 10^2$ at H_U, the upper point in Fig. 4 (b) (inset) where a stable limit cycle emerges via a supercritical Hopf bifurcation and $l_1 = 5.32 \times 10^4$ at the lower point H_L. We start the continuation analysis from a maximum value of $c_0 = 0.5 \, \mu$M where the fixed point is stable [top of the *blue curve* in Fig. 4 (a)] as shown by the negative real and zero imaginary parts of the eigenvalues of Jacobian [right hand sides of Figs. 4 (c) and (d)]. Upon decreasing c_0 we reach the H_U ($c_0 = 0.34 \, \mu$M) point where the stable limit cycle emerges; we observe limit cycles with larger amplitudes with the further decrease in c_0 (*blue cyclic trajectories* in Fig 4 (b)). The cyclic trajectory for the intermediate value of $c_0 = 0.16 \, \mu$M is shown in Fig. 3 (c). After reaching H_L point at $c_0 = 0.1585 \, \mu$M the unstable limit cycle occurs as marked by *red dashed cycles* of small amplitude in zoom of Fig. 4 (b). The stable cycle emerging from H_U collides with the unstable one emerging from H_L close to $c_0 = 0.158 \, \mu$M. This fold bifurcation of limit cycles is labeled by LPC (marked by *black dotted trajectory*). The limit cycle solution ceases to exist while decreasing c_0 value lower then LPC point. Thus, we conclude that the stable limit cycle solutions exist in a small range of $[\text{Ca}^{2+}]$ concentration between H_U and LPC points.

The bifurcation diagrams obtained from DYK [7] and Li-Rinzel [8] models are different from the one presented above, owing to different assumptions about the speed of dynamical variables and different reduction schemes employed. In [7] and [8] $[\text{Ca}^{2+}]$ and $[\text{IP}_3]$ are dynamical, whereas we keep $[\text{IP}_3]$ at a high constant level. Moreover, the earlier models assume a well-mixed membrane and do not account for the clustering of channels that was introduced in [23] setting the inactivation rate to be frozen at $\tilde{k}_i^+ = k_i^+ c_s$. We study the different Ca^{2+} dynamics associated with IP_3R clusters and physiological parameters for

which the transitions for different kinds of behavior may occur.

The phenomena described above shows the Ca^{2+} oscillations in a cytosolic $[Ca^{2+}]$ at a single cluster. The amplitudes of oscillations lie within a physiologically plausible range and their periods are similar to the oscillations found in several cells types [38]. However, various studies [12, 13] imply that Ca^{2+} oscillations are collective in nature, and emerge when multiple clusters are involved. In our model, we, therefore, cannot allow individual clusters to oscillate autonomously. We shall show how it is only via the coupling between clusters that oscillations emerge, and switching off the inter-cluster coupling leads to the loss of rhythmic behavior. Thus, we next study the behavior of Ca^{2+} release from arrays of clusters.

B. Cluster-based model of a discrete chain of clusters

Here we study the dynamics of a chain of clusters coupled by diffusing Ca^{2+} ions. Firstly, we start by analyzing a simple example to illustrate the effect of coupling between neighboring clusters. Consider L clusters coupled with the diffusion term in eq. (5). The discrete form of eq. (5) for the ith cluster is expressed in terms of the local Ca^{2+} concentration c_i whose rate of change is proportional to the spatial gradient of the diffusion current J_i for $i = 1, \ldots, L$. The continuum diffusion equation is derived from

$$\frac{\partial c_i}{\partial t} = \frac{1}{\ell}(J_i - J_{i-1}) = \frac{1}{\ell}\left[D\left(\frac{c_{i-1} - c_i}{\ell}\right) - D\left(\frac{c_i - c_{i+1}}{\ell}\right)\right]. \tag{7}$$

In our model with a discrete distribution of clusters, we shall take $\ell \approx 1.4\,\mu$m as the optimal distance between clusters adapted for the current model and D, the effective diffusion constant for Ca^{2+} ions is taken to be $D = 30\ \mu\text{m}^2/\text{s}^{-1}$ [39]. Here we assume the clusters to be arranged in a ring topology, $c_{i+L} = c_i$. We numerically solve the system (1), (2) and (5) assuming the diffusion term as in eq. (7) and model parameters as in the previous section. Only the equilibration rate is modified for these simulations and set to $\lambda = 230\,\text{s}^{-1}$, instead of $\lambda = 10^3\,\text{s}^{-1}$ that was used earlier.

Here we consider the discrete lattice model for $L = 2$, a typical unit cell of a discrete chain of clusters. The model parameters for both clusters are the same apart from the activatable numbers of channels in clusters, which are $N = 9$ ($N = 5$) in the first (second) cluster. In

this case, our model is given by

$$\frac{\mathrm{d}a_i}{\mathrm{d}t} = f(a_i, h_i, c_i), \ i = 1, 2 \tag{8}$$

$$\frac{\mathrm{d}h_i}{\mathrm{d}t} = g(a_i, h_i, c_i), \ i = 1, 2 \tag{9}$$

$$\frac{\mathrm{d}c_1}{\mathrm{d}t} = -\lambda[c_1 - c_d(a_1)] - \frac{2D}{\ell^2}(c_1 - c_2), \tag{10}$$

$$\frac{\mathrm{d}c_2}{\mathrm{d}t} = -\lambda[c_2 - c_d(a_2)] - \frac{2D}{\ell^2}(c_2 - c_1). \tag{11}$$

We present the results of this unit cell $L = 2$ model in Fig. 5 (a), (b) and (c). Note, that the unit cell case is a particular example of a chain of clusters of length L. We use the discrete chain approximation to illustrate the behavior of the clusters in a "one-dimensional membrane".

Unlike the single-cluster approach, calcium concentration c in the cytosol is explicitly added to the model, the equilibration rate λ is reduced and the diffusion term is introduced in eqs. (10), (11). The assumption that c will be "slaved" to c_d is inapplicable; we need to account for a separate dynamics of Ca^{2+} cytosolic concentration away from the steady-state value c_d.

The oscillatory trajectories are exhibited in clusters 1 [Fig. 5 (a)] and 2 [Fig. 5 (b)] as the consequence of a diffusive interaction between the clusters. Notably, the concentration of Ca^{2+} at cluster 1 exhibits small amplitude oscillations [Fig. 5 (c) *top*] around the fixed point with high c_1 [here the fixed point is associated with the higher fixed point in Fig. 3 (b) for the single cluster case but now we solve the 6–variable system]. The influx from the cluster 1 causes the emergence of Ca^{2+} oscillations in cluster 2 [Fig. 5 (c) *bottom*]. In order to study this effect, we perform the continuation analysis of the system of two coupled clusters given by eqs. (8)–(11) similarly to a single cluster approach described earlier. The dimensionality of the system used in the bifurcation analysis remains 6, but we represent the results as two (three) dimensional plots to depict the governing dynamics at each cluster. We plot the bifurcation diagram shown in Fig. 5 (d) which represents the dependence of the a_2 value of the fixed point versus D as the control parameter. The effect of Ca^{2+} flux from cluster 1 to cluster 2 is proportional to D which controls the strength of coupling. We observe a similar diagram as shown in Fig. 4. We also observe H_U and H_L points where stable and unstable limit cycles occur, respectively. From the eigenvalues plotted in Fig. 5 (f), we confirm that H_U and H_L are Hopf bifurcation points. The continuation of the stable limit
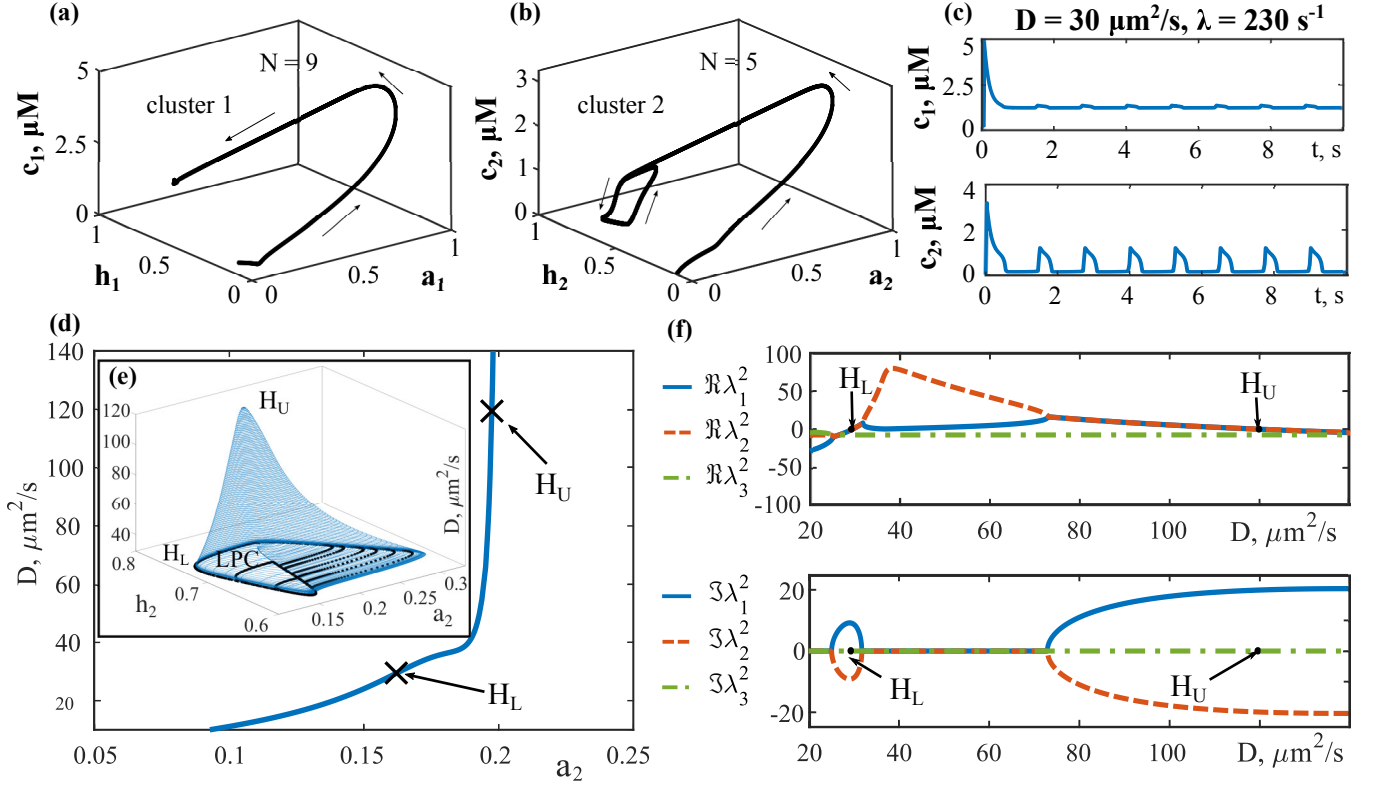
FIG. 5: (Color online) The initiation of Ca^{2+} oscillations in the array of two clusters $D = 30\,\mu m^2/s$, $\lambda = 230\,s^{-1}$. **(a)** The trajectory in cluster 1 with $N = 9$ channels. **(b)** The oscillatory trajectory in cluster 2 ($N = 5$) triggered by the diffusion from the first cluster. **(c)** Oscillating Ca^{2+} profiles in both clusters. **(d)** Bifurcation diagram of the system of two coupled clusters plotted versus diffusion coefficient D. The points H_L and H_U represent Hopf bifurcation points ($\Re\lambda = 0$, $\Im\lambda \neq 0$). **(e)** The continuation of a limit cycle (blue lines) performed by analogy to Fig. 4 (b) varying D. Similarly, the black markers correspond to the fold bifurcation of limit cycles (LPC). **(f)** The real (*top*) and imaginary (*bottom*) parts of the eigenvalues of the system.

cycle occurring at H_U [Fig. 5 (e)] shows that the periodic solutions in the cluster 2 exist in the range $(29 \leq D \leq 120)\,\mu m^2/s$. This brings the range of concentrations of Ca^{2+} to the one shown in Fig. 4 for the same λ. Thus, we conclude that the emergence of oscillations in the second cluster depends on the concentration influx from cluster 1 to cluster 2 which raises the level of concentration in cluster 2 to a range that drives oscillations in the single cluster approach.

Having accounted for the ability of diffusive couplings to bring about oscillations in a

coupled cluster system when the individual clusters exhibit non-oscillatory dynamics on their own, we extend the model to a continuum description. In the next subsection, we apply this mechanism to a domain of the membrane in order to qualitatively demonstrate the emergence of Ca^{2+} waves and oscillations in the ER membrane.

C. Calcium Waves and Oscillations in the cluster-based model

As shown above, the behavior of the three-state model for a single cluster depends on the number of channels N in a cluster that are IP_3 bound and may be activated or deactivated by Ca^{2+}, namely, excitable for small N transitioning for large N to bistable dynamics. While the ER membrane would typically contain clusters of different numbers of channels, we study the simplest heterogeneous scenario with one bistable cluster with $N = 9$ and the multiple excitable clusters with $N = 5$. Here and furthermore we refer to a $N = 9$ cluster as bistable and a $N = 5$ cluster as excitable as per their behavior in the isolated single cluster case, even though it is the entire system whose stability matters. The choice of this figures is based on the study [24], where the average number of activatable channels in *Xenopus* oocytes ER membranes tend to $N = 5$ with the increase in $[IP_3]$, the distribution of numbers of channels appears to be very close to a Poisson distribution [3, 24]. We chose this numbers to be consistent with [24] and propose the modeling of more complex heterogeneous systems for future study. In the chosen situation the excitable behavior may be associated with short-lasting puffs while the bistable behavior may be associated with waves or long-lasting puffs, where the exit from the long-lasting puffs that is thought to be driven by dissociation of IP_3 or other mechanisms which are discussed in subsection III D. The exit from the long elevated high Ca^{2+} concentrations might be performed through the other mechanisms such as change in coupling strength α, maximal Ca^{2+} elevation c_s or transition rate k_i^+.

In this section, we model a domain of an ER membrane which is assumed to contain multiple excitable clusters ($N = 5$) and the only one bistable ($N = 9$) cluster in order to study the interplay between excitable and bistable clusters. We demonstrate the emergence of oscillations and quantify the characteristics of the phenomena such as front velocity and period.

We numerically solve the eqs. (1), (2) and (5) in the chosen one-dimensional domain with open boundaries and Neumann boundary conditions $c_x'(x = 0, L) = 0$. Let us assume

the part of ER membrane with the initial distribution of cytosolic $[\text{Ca}^{2+}]$ $c(x,0) = c_0 + A\exp\{-[x^2/(2\sigma^2)]\}$, where $A = 2\,\mu\text{M}$, $\sigma = 0.1\,\mu\text{m}$, which travels from the left part of a membrane as shown in Fig. 6 (a). Calcium release upon activation occurs only at channel clusters i in eq. (5) via $c_d(a)$ and cytosolic concentration of Ca^{2+} is raised above basal level c_0 by diffusion between clusters a constant distance $\ell = 3.5\,\mu\text{m}$ apart. The results depicted in Fig. 6 are obtained for equilibration rate $\lambda = 230\,s^{-1}$. The effect of changing the values of D, λ, and ℓ upon qualitatively differing Ca^{2+} release response is discussed further in this section.
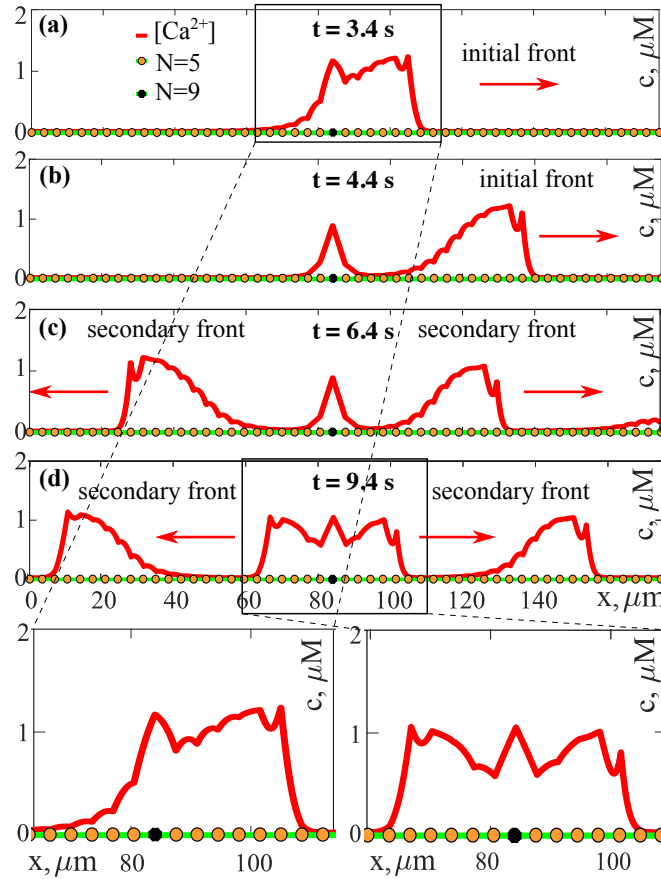

FIG. 6: (Color online) Ca^{2+} front propagation from the spatial model for two types of clusters ($D = 30\,\mu\text{m}^2/\text{s}$, $\lambda = 230\,\text{s}^{-1}$). The *orange dots* represent excitable clusters with $N = 5$ channels as long as the *large black dot* corresponds to a bistable cluster with $N = 9$ channels. **(a)** The propagation of a front caused by the raised initial $[\text{Ca}^{2+}]$ in the left part of the membrane. **(b)** The Ca^{2+} peak occurs at the bistable cluster. **(c)** The diffusion from the peak causes initiation of a secondary wave. **(d)** The front propagates after that subsequent front occurs. The waves occur periodically from the bistable cluster.

In Figs. 6 (c) and (d) we observe the emergence of Ca^{2+} oscillations at the bistable cluster (*black dot*) triggered by the initial front [Fig. 6 (a)]. The front occurs from an initial Ca^{2+} increase close to the point $x = 0\,\mu m$ and diffuses throughout the membrane. While the initiation event is set by choosing initial condition in our deterministic model it reflects the potential occurrence of an initial peak by either an internal or external stimulus or a stochastic fluctuation. After passing the bistable cluster the initial front raises the concentration at this cluster to the value of c which corresponds to the upper fixed point in Fig. 5 (a). This behavior induces a long-lasting state which is terminated by IP_3 unbinding, a feature which we discuss later. Therefore, in Fig. 6 (b) a residual peak occurs at cluster $N = 9$. Thereafter, two secondary fronts emerge from the residual peak as shown in Fig. 6 (c). As we consider deterministic oscillations this process repeats periodically with a constant period [Fig. 6 (d)].

This behavior can be observed because of two different regimes underlying Ca^{2+} release in clusters: excitable for short-lasting puffs and bistable for long-lasting events. Our model shows that bistable clusters can produce long-lasting puffs that might cause the emergence of Ca^{2+} oscillations in cellular membranes.

The diffusion coefficient D and relaxation parameter λ incorporate spatial effects without explicitly modeling buffers in the membrane. As these are likely to influence the characteristics of the Ca^{2+} waves and oscillations we vary D to study how these characteristics change. Furthermore, by changing equilibration rate λ we can model the inclusion of a linearized reaction Ca^{2+} leak flux and pump action terms in the eq. (5). There are different timescales for the activation and inhibition of the channels "hidden" in eqs. (1), (2). The action of pumps occurs on much slower timescales compared to λ chosen.

In Fig. 7 (a) we show the values of the average time calculated between two subsequent Ca^{2+} release events at each cluster. This value appears to be almost constant. We map the change in a period of Ca^{2+} oscillations to physiological ranges of D and λ [Fig. 7 (a)]. Dark regions correspond to a non-oscillatory response, while oscillations occur within the purple triangular zone. A curious effect is observed at the lower edge of the triangle in the range $(100 \leq \lambda \leq 200)\,s^{-1}$. The light spots marked by white circles correspond to the region on the diagram where oscillations exhibit periods ≈ 10 s and belong to Ca^{2+} alternans – a pulse travels alternately to the right, followed by another to the left and so on (Fig. S2). Under given initial conditions, this effect can be explained by the fact that the concentration

TABLE II: Parameters used in the cluster-based reaction-diffusion model.

Parameter	Value	Description
c_0	$0.025\,\mu$M	Rest level of [Ca^{2+}]
N	5 or 9	Number of activatable channels
		in a cluster (IP$_3$ bound)
λ	$230\,\text{s}^{-1}$	Equilibration rate
D	$30\,\mu\text{m}^2/\text{s}$	Diffusion coefficient
ℓ	$3.5\,\mu$m	Inter-cluster distance
r_{cl}	$0.1\,\mu$m	Cluster radius

diffusing from the irregular cluster is sufficient to excite a neighboring cluster only from one side at a time. Thus, we observe the oscillations occurring on alternate sides of the bistable cluster sequentially. In Fig. 7 (b) we show the velocity of propagation of the initial front for a similar range of D and λ: the dark regions corresponding to abortive waves or puffs and the light trapezium corresponds to propagating Ca^{2+} waves.

The distance between clusters in the various cell types lies in range $1 - 7\,\mu$m [40]. Figs. 7 (c) and (d) show the dependence of the periods and the velocities on λ for different values of the distance ℓ between the clusters. In both graphs, we consider the effective diffusion constant to be fixed at a typical value of $D = 30\,\mu\text{m}^2/\text{s}$. The periods of the oscillations [Fig. 7 (c)] generally reach larger values for long distances between clusters. This can be explained by the fact that the front travels a longer distance in order to reach neighboring clusters. Interestingly, the oscillatory behavior exists in wider ranges of λ for smaller distances between the clusters [Fig. 7 (c)]; oscillations are more robust to the equilibration process if the distances between clusters are smaller. The same processes define the velocities [Fig. 7 (d)]; these are higher for shorter distances because a front reaches a neighboring cluster faster and is able to trigger a response there. The data with comparatively large periods $\approx 4 - 5\,\text{s}$ for $\ell = 5\,\mu$m, $\ell = 4\,\mu$m and $\ell = 3\,\mu$m in Fig. 7 (c) exhibits the non-regular alternans emerging similarly as in Fig. 7 (a).
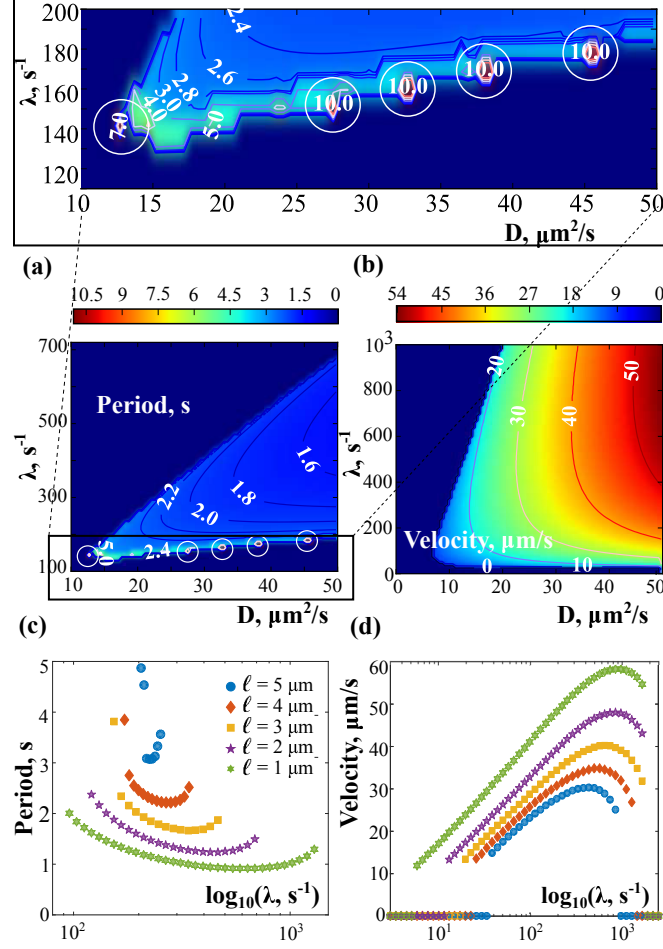
FIG. 7: (Color online) **(a)** The phase diagram which represents different kinds of Ca^{2+} dynamics such as puffs, waves, and oscillations. The domain with zero periods [*dark-blue zone* in (a)] contains both puffs and waves in a co-existing manner. The *triangular light-blue domain* with non-zero periods contains oscillatory behavior of the system. The *white circles* indicate the regions with Ca^{2+} alternans. **(b)** The phase diagram representing two regimes of Ca^{2+} dynamics such as puffs and waves in the case when all the clusters are excitable. Zero velocity domain in *dark-blue* corresponds to puffs and abortive waves, while the non-zero-velocity domain (shown in *blue* to *red* colors) represents waves. **(c)** The dependence of the period on λ for different inter-cluster distances, $D = 30\,\mu\mathrm{m}^2/\mathrm{s}$. **(d)** The dependence of velocity on λ, the distances, and the diffusion coefficient are the same as in (c).
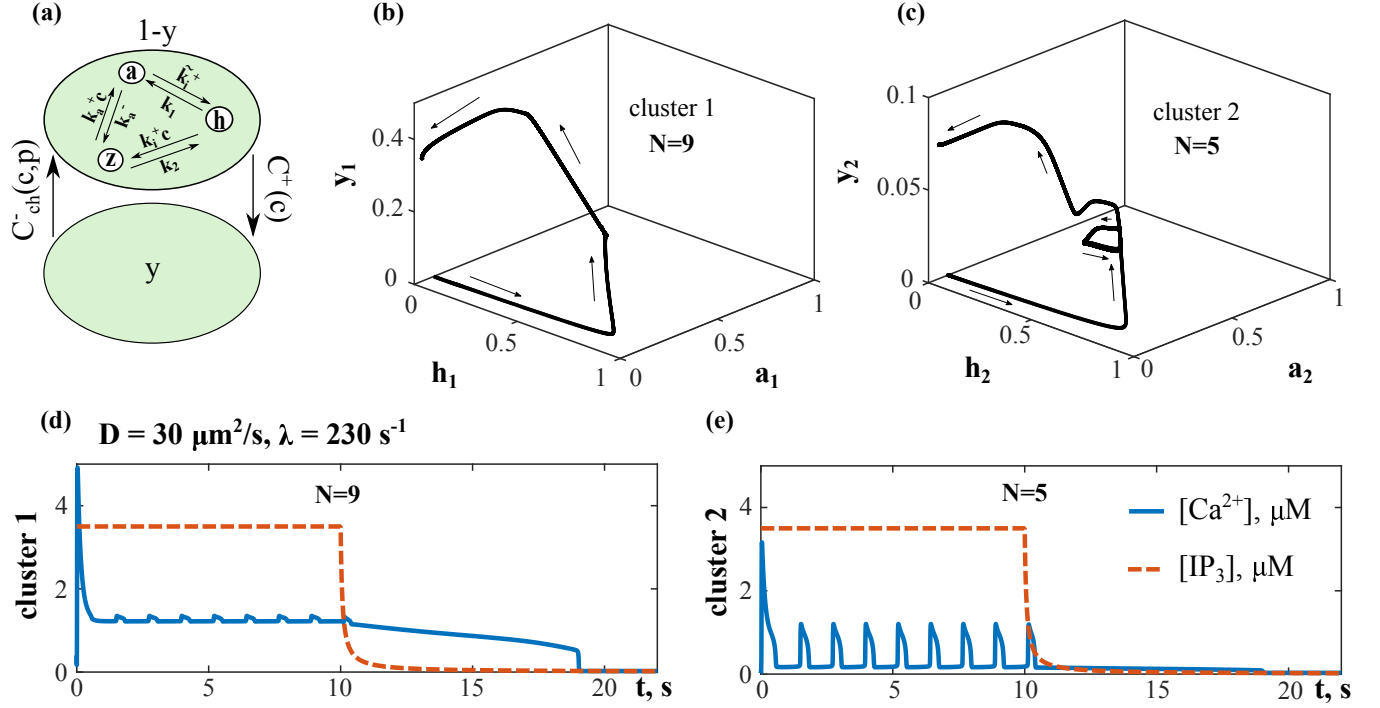
FIG. 8: (Color online) The IP$_3$ dependent model for two coupled clusters. **(a)** The scheme of an extension of the three-state model introduced in Fig. 1 (c). The transitions between the upper and the lower plane of the DYK cube are governed by the steady-state rates C^+ and C_{ch}^- in analogy to Li-Rinzel [8]. **(b)**, **(c)** The trajectories in the (a, h, y) phase space, where y corresponds to the fraction of the channels in a cluster occupying the lower plane of the DYK cube, N is the number of activatable channels in a cluster. **(d)**, **(e)** The oscillatory regime corresponding to Fig. 5 (*blue solid lines*) for high [IP$_3$] is terminated due to the decrease in the [IP$_3$] (*red dashed lines*).

D. IP$_3$ dependence

The assumption of high levels of [IP$_3$] leads to a sustained Ca^{2+} release from the bistable cluster. In the current subsection, we aim to link the termination of this event to the change in the [IP$_3$] levels [*red dashed lines* in Figs. 8 (d), (e)] on timescales slower than the oscillations found in previous subsections [*blue solid lines* in Figs. 8 (d), (e)].

The extension of the model is sketched in the Fig. 8 (a). In the case of two coupled

clusters the IP$_3$ dependent model (8), (9) reads as

$$\frac{\mathrm{d}a_i}{\mathrm{d}t} = f_p(a_i, h_i, y_i, c_i), \ i = 1, 2 \tag{12}$$

$$\frac{\mathrm{d}h_i}{\mathrm{d}t} = g_p(a_i, h_i, y_i, c_i), \ i = 1, 2 \tag{13}$$

$$\frac{\mathrm{d}y_i}{\mathrm{d}t} = C^+(c_i)(1 - y_i) - C_{\mathrm{ch}}^-(c_i, p)y_i, \tag{14}$$

where f_p and g_p are given in eqs. (A34) and (A35), C^+ and C_{ch}^- are given in eqs. (A23) and (A29), respectively. The IP$_3$ changes as

$$p(t) = \begin{cases} p_0, & \text{if } t \leq t_{\mathrm{dur}}, \\ \frac{p_a \sigma_0^2}{\sigma_0^2 + 2D_p t} \, \mathrm{e}^{\frac{-x^2 - y^2}{4D_p t + 2\sigma_0^2}}, & \text{otherwise}, \end{cases} \tag{15}$$

where the initial value of [IP$_3$] at a cluster $p_0 = 3.5\,\mu$M, the duration of the IP$_3$ stimulus is $t_{\mathrm{dur}} = 10\,$s. We assume the shape of the initial [IP$_3$] distribution to be Gaussian of amplitude $p_a = 4.6\,\mu$M and with variance $\sigma_0^2 = 1\,\mu$m^2 (see Supporting Material Sec. S3). After stimulus terminates, [IP$_3$] diffuses in infinite 2D domain ($D_p = 10\,\mu$m^2/s [41]). We calculate time traces shown by *red dashed lines* in Fig. 8 (d) and (e) at clusters positioned at $x = \pm(\ell + r_{cl})/2$ and $y = 0$ (here the distance between clusters $\ell = 1.4\,\mu$m, cluster radius $r_{cl} = 0.1\,\mu$m). Ca^{2+} dynamics remains unaltered as in eqs. (10), (11).

The trajectories in (a, h, y) phase space for both clusters are exhibited in Figs. 8 (c), (d). The global oscillations occur in our model at [IP$_3$]$\approx 3 - 4\,\mu$M, which is compatible with the levels considered in [42]. The termination of the oscillations [solid blue lines in Fig. 8 (e), (d)] at both clusters is caused by the decrease in [IP$_3$] under a level of several tens of nM, which is typically taken as the rest value of the [IP$_3$] [24]. It might be useful to reconsider the influence of the calcium pumps in the termination process as we had argued that their effects are subsumed in a linearized equilibration rate λ. We have checked that the effect of introducing an explicit pump term [7] on the wave termination behavior can be accommodated by adjusting λ.

IV. DISCUSSION AND CONCLUSIONS

In this paper, we presented a reaction-diffusion model of a membrane containing clusters of IP$_3$ receptor channels of the fire-diffuse-fire [21] type but with a mechanistic description

27

of channel firing similar to the spatial Fitzhugh-Nagumo model [43, 44]. This mechanistic model was built on top of a dynamical systems analysis of a previously proposed simplification [23] of the DYK model [7]. We noticed that incorporating the transition rates given in [24] into the model revealed the emergence of Ca^{2+} oscillations even in a single cluster which inspired the membrane level formulation of a model of Ca^{2+} puffs, waves, and oscillations whose characteristics were quantified under varying cluster configurations and physiological conditions. Our model allows us to observe Ca^{2+} waves with the velocities in agreement with experiments by Marchant et al. [42] for various distances between clusters and equilibration rates [Figs. 7 (b) and (d)].

Here we propose the mechanism of initiation of oscillatory behavior in the membrane that consists of the following sequence.

- Upon receiving an IP_3 stimulus the membrane configures IP_3 receptor channels to form clusters with different numbers of channels [3] with bound IP_3 that are primed for activation by Ca^{2+} binding.

- If the number of primed channels in a cluster is higher than a threshold value, then the cluster is bistable. When an initial surge of Ca^{2+} passes the bistable cluster [Fig. 6 (b)] it drives Ca^{2+} concentration there into the higher fixed point of the dynamics as shown in Fig. 5 (a). Sustained Ca^{2+} elevation at a bistable cluster corresponds to a long-lasting release event.

- The residual $[Ca^{2+}]$ at the bistable cluster diffuses to the neighboring clusters.

- This drives $[Ca^{2+}]$ at the neighboring clusters into an oscillatory regime as in Fig. 5. These oscillations spread to further clusters due to diffusive coupling.

It is generally known that high Ca^{2+} concentrations might lead to cell death and this renders the presence of bistability and consequent sustained Ca^{2+} release in our model an unhappy feature. Due to fast luminal Ca^{2+} refilling [45] sustained Ca^{2+} release, such as what follows from a transition to the upper fixed point of the bistable regime, cannot be terminated by ER depletion at the timescales considered by current paper. The mechanistic origins of our model enable us to propose possible physiological possibilities that might explain the termination of Ca^{2+} release from the bistable cluster.

- *IP_3 unbinding.* In the full DYK approach, Rüdiger et al. [32] attribute the termination of long-lasting Ca^{2+} release events to IP_3 unbinding. A simplified model with inclusion of the lower plane of the DYK cube shown in subsection III D has also displayed the termination of a Ca^{2+} wave in the bistable cluster in Fig. 8. Thus, we argue that neglecting IP_3 unbinding completely might lead to results which seem unrealistic. Therefore, the limits of the applicability of our model are bound to the change of the IP_3 levels in the cell.

- *The uncoupling of IP_3R channels.* Our bifurcation analysis shows that the system ceases to be bistable if the coupling between channels α decreases. Hence, if α decreases on timescales slower than oscillation periods observed in the model, the long-lasting event can terminate (see Fig. 9). In this paper, we have considered α to be constant, which might not always be the case in real clusters. It is known from experiments that the coupling (uncoupling) of IP_3R channels is caused by IP_3 binding (unbinding) [3, 46, 47]; the mechanisms which connect channels remain largely unknown, however. If an increase in p leads to a fast (hundreds of ms according to [47]) increase in coupling strength α could acquire a value as taken in this paper. Following the initial stimulus that triggers this increase of IP_3 and its consequent effect on α, a gradual diminution of IP_3 levels could still restrict the dynamical states to the upper place of the DYK cube, while reducing the coupling between channels in a cluster. This would lead to the termination of puffs on the timescales defined by the change in $[IP_3]$ levels. However, only decreasing α under 0.1 [Fig. 9 (a)], which corresponds to a Ca^{2+} concentration at a single cluster, leads to the exit from the bistable state. A mechanism which causes decoupling of channels in large clusters has been discovered in the RyR clusters [48] although a similar property has not been reported for IP_3 receptors.

- *ER depletion.* In this study, we assume the same availability of Ca^{2+} in the luminal pool in (4). Even though the ER pool can be large and its fast refilling can prevent local depletion [45], other studies suggest that the large pool can be completely depleted by high-amplitude sustained Ca^{2+} releases [49].

- *Stochastic termination.* The bistability found in the single-cluster model can also be terminated stochastically. Fig. 10 shows the distribution of inter-puff intervals (IPIs) obtained from the Langevin model based on eqs. (1)–(2). We consider the additive
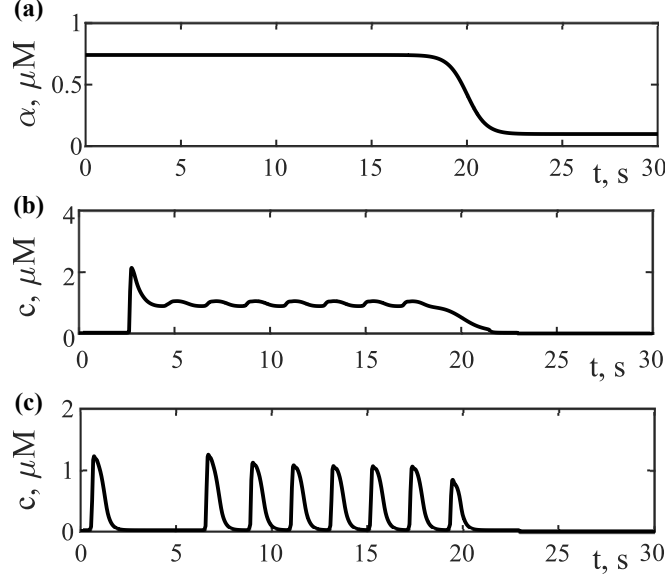
FIG. 9: **(a)** The change of the coupling strength α in eq. (4) on a slow timescale caused by the uncoupling of IP$_3$R channels due to IP$_3$ unbinding. **(b)** The termination of the sustained Ca^{2+} release at the bistable cluster shown in Fig. 6. **(c)** The termination of the oscillatory Ca^{2+} release in one chosen excitable cluster shown in the Fig. 6.

Wiener noise as shown in (B1), (B2) and compare the results with experimental puff data [5]. The duration of the events lies in a range of hundreds of ms which is also consistent with the experimental data available.

There are other consequences for the fixed levels of IP$_3$ in the model. Due to the fixed high level of [IP$_3$] assumed, our model exhibits periods of oscillations lower than the wide range found in typical experimental studies. Although the high IP$_3$ assumption narrows the range of periods observed, it helps us to study the main characteristics of waves and oscillations phenomenologically. The variability of the periods can be achieved by incorporating more complex features of Ca^{2+} signals such as stochasticity [12, 13] and array enhanced coherence resonance [11] under dynamical [IP$_3$] loads.

There are other characteristics of the emergent Ca^{2+} waves and oscillations in our model that matches those reported in the extensive experimental literature [38, 42, 50, 51]. In particular, Marchant and Parker [51] have shown that an increase in [IP$_3$] shortens intervals between Ca^{2+} release events. Our model agrees with these experiments by exhibiting oscillations with frequency increasing with increase in [IP$_3$]. The periods of oscillations are also consistent with Rückl. et al. [24]. The amplitudes of oscillations are in a range of observed
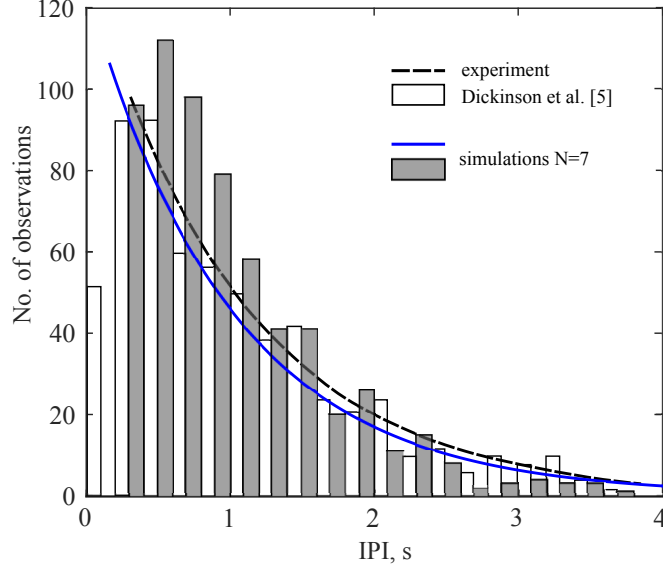
30

FIG. 10: (Color online) Inter-puff intervals of the stochastic single-cluster model (B1), (B2), (3) containing $N = 7$ channels with additive Wiener noise. *Grey bars* are fitted with the *blue solid* curve and represent the distribution of IPIs obtained from the modeling of 622 puffs. *White bars* with *black solid* fit are reproduced from the experiments reported in [5].

puffs and waves [52]. Also, the effect of wave collision found experimentally is present in our model.

In this paper, a reduced description of clustered channels with a parametric representation of the dynamics of subunits of channels is present alongside membrane-level diffusion-enabled interactions. While the simplifications introduced in the reduction scheme can lead to model behavior inconsistent with empirical observations, the dynamical systems analysis presented here as a means of linking phenomena at different scales also enables us to propose explanatory mechanisms that could be accommodated in more elaborate models.

See Supplemental Material at [URL] for the extended bifurcation analysis of the single-cluster model (Subsec. III A), the figure illustrating alternans (Subsec. III C), the change of IP_3 (Subsec. III D) derived from diffusion equation.

ACKNOWLEDGMENTS

Appendix A: DYK reduction to the three-state model

The kinetics governing the upper plane of DYK cube [Fig. 1 (b)] is formulated as the next set of differential equations

$$\dot{x}_{110} = -x_{110}(b_1 + a_2c + b_5) + x_{010}a_1p +$$
$$+x_{111}b_2 + x_{100}a_5c, \tag{A1}$$
$$\dot{x}_{100} = -x_{100}(b_1 + a_2c + a_5c) + x_{000}a_1p +$$
$$+x_{101}b_2 + x_{110}b_5, \tag{A2}$$
$$\dot{x}_{101} = -x_{101}(b_2 + a_2c + a_5c) + x_{100}a_2c +$$
$$+x_{001}a_3p + x_{111}b_5, \tag{A3}$$
$$\dot{x}_{111} = -x_{111}(b_2 + b_3 + b_5) + x_{110}a_2c +$$
$$+x_{011}a_3p + x_{101}a_5c, \tag{A4}$$

where $x_{110} + x_{100} + x_{101} + x_{111} = 1 - y$, $y = x_{000} + x_{001} + x_{011} + x_{010}$. The fractions of subunits in state ijk are denoted as x_{ijk}.

In the case of high [IP$_3$] the IP$_3$ binding sites are saturated. Therefore, we can apply the condition of detailed balance between upper and lower planes of DYK: $a_ipx_{0jk} = b_ix_{1jk}$ for four sets of i, j, and k such as $i = 1$, $j = 0, 1$, $k = 0$ and $j = 3$, $j = 0, 1$, $k = 1$. From these conditions we derive

$$x_{000} = \frac{x_{100}b_1}{a_1 p}, \tag{A5}$$

$$x_{010} = \frac{x_{110}b_1}{a_1 p}, \tag{A6}$$

$$x_{001} = \frac{x_{101}b_3}{a_3 p}, \tag{A7}$$

$$x_{011} = \frac{x_{111}b_3}{a_3 p}. \tag{A8}$$

We substitute eqs. (A5)–(A8) into the system of eqs. (A1)–(A4). The resulting four state model appears as

$$\dot{x}_{110} = -x_{110}(a_2 c + b_5) + x_{111}b_2 + x_{100}a_5 c, \tag{A9}$$

$$\dot{x}_{100} = -x_{100}(a_2 c + a_5 c) + x_{101}b_2 + x_{110}b_5, \tag{A10}$$

$$\dot{x}_{101} = -x_{101}(b_2 + a_5 c) + x_{100}a_2 c + x_{111}b_5, \tag{A11}$$

$$\dot{x}_{111} = -x_{111}(b_2 + b_5) + x_{110}a_2 c + x_{101}a_5 c, \tag{A12}$$

where $x_{110} + x_{100} + x_{101} + x_{111} = 1 - y$ due to conservation of probability, $y = x_{010} + x_{000} + x_{001} + x_{011}$.

Now we introduce a reduction of DYK similarly to Li and Rinzel [8]. However, here we separate the upper and lower planes of the DYK cube [Fig. 1 (a)]. Considering the lower plane of the DYK cube in a steady state we obtain

$$x_{000} = \frac{d_5 d_4 y}{(c + d_5)(c + d_4)}, \tag{A13}$$

$$x_{001} = \frac{d_5 c y}{(c + d_5)(c + d_4)}, \tag{A14}$$

$$x_{010} = \frac{d_4 c y}{(c + d_5)(c + d_4)}, \tag{A15}$$

$$x_{011} = \frac{c^2 y}{(c + d_5)(c + d_4)}, \tag{A16}$$

where $d_i = b_i/a_i$, $i = \overline{1,5}$.

Similarly, the upper plane is in a steady state gives

$$x_{100} = \frac{d_5 d_2 (1-y)}{(c+d_5)(c+d_2)}, \tag{A17}$$

$$x_{101} = \frac{d_5 c (1-y)}{(c+d_5)(c+d_2)}, \tag{A18}$$

$$x_{110} = \frac{d_2 c (1-y)}{(c+d_5)(c+d_2)}, \tag{A19}$$

$$x_{111} = \frac{c^2 (1-y)}{(c+d_5)(c+d_2)}. \tag{A20}$$

To calculate the transition rates between these two groups we use steady state equations for upper plane (A14)–(A16) and lower plane (A18)–(A20)

$$
\begin{aligned}
K^- &= a_1 p (x_{000} + x_{010}) + a_3 p (x_{001} + x_{011}) = \\
&= \frac{(a_3 c + a_1 d_4) p y}{c + d_4},
\end{aligned} \tag{A21}
$$

$$
\begin{aligned}
K^+ &= b_1 (x_{100} + x_{110}) + b_3 (x_{101} + x_{111}) = \\
&= \frac{(b_3 c + b_1 d_2)(1 - y)}{c + d_2},
\end{aligned} \tag{A22}
$$

here we define transition rates between upper and lower planes of the DYK cube as

$$C^+ = \frac{b_3 c + b_1 d_2}{c + d_2}, \ C^- = \frac{(a_3 c + a_1 d_4) p}{c + d_4}, \tag{A23}$$

which is used in (14), the corresponding transition rates are given in Tab. III.

The results presented by the system of eqs. (A9)–(A12) are applicable to a subunit of a channel. In order to describe the behavior of a cluster of channels, similarly to [23], we introduce variables a, g, h' and z that represent fractions of channels in states 110, 111, 101, and 100, respectively. Thus including the IP$_3$ dependence the system (A10)–(A12) transforms to

$$\frac{\mathrm{d}a}{\mathrm{d}t} = k_a^+ c z - k_a^- a + k_i^- g - \tilde{k}_i^+ a, \tag{A24}$$

$$\frac{\mathrm{d}g}{\mathrm{d}t} = k_a^+ c h' - k_a^- g - k_i^- g + \tilde{k}_i^+ a, \tag{A25}$$

$$\frac{\mathrm{d}h'}{\mathrm{d}t} = k_a^- g - k_a^+ c h' + k_i^+ c z - k_i^- h', \tag{A26}$$

$$\frac{\mathrm{d}y}{\mathrm{d}t} = C^+ (1 - y) - C_{\mathrm{ch}}^- y, \tag{A27}$$

where $z = 1 - a - g - h' - y$ as sum of the fractions of all states to unity, y defines the fraction of IP$_3$R unbound channels (occupying the lower plane of the DYK cube), C^+ and C_{ch}^- are given by eqs. (A23) and (A29), respectively.

The kinetics of these variables is governed by rates $k_a^\pm$, $k_i^\pm$ and concentrations c and c_s, where we substitute two parameters k_i^+ and c_s as $\tilde{k}_i^+ = k_i^+ c_s$. These transition rates are obtained from the original DYK rates. Earlier simulations [23] showed that most of the reactions (k_a^-, k_i^+, and k_i^-) in the four-state model are obtained from b_5, a_2, and b_2, respectively. In contrast, k_a^+ rate has been constructed from the condition of channel opening (at least three subunits should be active). The probability of the single subunit activated is $P_{\text{act}} = a_5 c/(a_5 c + b_5)$. According to the binomial distributions, the probability of none of the subunits is active is $P_0 = (1 - P_{\text{act}})^4$. If only one of four subunits is active and all remaining ones are inactive $P_1 = 4 P_{\text{act}} (1 - P_{\text{act}})^3$. There are $C_4^2 = \frac{4!}{2!2!} = 6$ ways for two of four subunits to be activated, thus, $P_2 = 6 P_{\text{act}}^2 (1 - P_{\text{act}})^2$. Therefore, the transition to this state is possible only after the activation of two subunits. The probability that two subunits are active under the condition that the channel is closed is $P(2|\{0, 1, 2\}) = P_2/(P_0 + P_1 + P_2)$.

TABLE III: The parameters of the IP$_3$ dependent model adapted from [24, 25].

Parameter	Value
First order rates, μM$^{-1} \times$ s^{-1}	
a_1	2
a_3	4
a_4	1
Second order rates, s^{-1}	
b_1	2×10^{-3}
b_3	8
b_4	3.9×10^{-2}
Dissociation constants $d_i = b_i/a_i$, μM	
d_1	0.001
d_3	2
d_4	0.039

We calculate k_a^+ as a transition rate from a closed channel with two active subunits to an open channel with three activated subunits. One of two remaining inactive subunits might be activated, thus, we obtain

$$k_a^+ = 2a_5 P(2|\{0,1,2\}). \tag{A28}$$

Similarly to k_a^+ we derive C_{ch}^- which requires four subunits to bind IP$_3$ [26]

$$C_{\mathrm{ch}}^- = C^- P_{\mathrm{IP}}(3|\{0,1,2,3\}), \tag{A29}$$

where C^- is given by eq. (A23), $P_{\mathrm{IP}}(3|\{0,1,2,3\}) = P_3^{\mathrm{IP}}/(P_0^{\mathrm{IP}} + P_1^{\mathrm{IP}} + P_2^{\mathrm{IP}} + P_3^{\mathrm{IP}})$, similarly $P_{\mathrm{act}}^{\mathrm{IP}} = C^-/(C^+ + C^-)$, $P_0^{\mathrm{IP}} = (1 - P_{\mathrm{act}}^{\mathrm{IP}})^4$, $P_1^{\mathrm{IP}} = 4P_{\mathrm{act}}^{\mathrm{IP}}(1 - P_{\mathrm{act}}^{\mathrm{IP}})^3$, $P_2^{\mathrm{IP}} = 6(P_{\mathrm{act}}^{\mathrm{IP}})^2(1 - P_{\mathrm{act}}^{\mathrm{IP}})^2$, $P_3^{\mathrm{IP}} = 4(P_{\mathrm{act}}^{\mathrm{IP}})^3(1 - P_{\mathrm{act}}^{\mathrm{IP}})$.

In order to reduce the number of variables, similarly to [23] we introduce a compound state h which contains g and h' [Fig. 1 (d)]. The effective rates of transitions to this state are obtained from a detailed balance between g and h'. We introduce the fraction of channels in the compound state as the sum of components $h = g + h'$, where from detailed balance

$$h = \frac{k_a^-}{k_a^+ c} g + g = \frac{k_a^+ c + k_a^-}{k_a^+ c} g, \tag{A30}$$

$$h = h' + \frac{k_a^-}{k_a^+ c} h' = \frac{k_a^+ c + k_a^-}{k_a^-} h'. \tag{A31}$$

Considering that the rates of transition to compound state are

$$k_1 = k_i^- \frac{k_a^+ c}{k_a^+ c + k_a^-} = k_i^- g_0, \tag{A32}$$

$$k_2 = k_i^- \frac{k_a^-}{k_a^+ c + k_a^-} = k_i^- (1 - g_0), \tag{A33}$$

where $g_0 = k_a^+ c/(k_a^+ c + k_a^-)$.

The resulting model reads as

$$\begin{aligned}
\frac{\mathrm{d}a}{\mathrm{d}t} &= k_a^+(c)(1 - a - h - y) - k_a^- a + k_1(c)h - \tilde{k}_i^+ a \\
&\triangleq f_p(a,h,y,c),
\end{aligned} \tag{A34}$$

$$\begin{aligned}
\frac{\mathrm{d}h}{\mathrm{d}t} &= k_i^+ c(1 - a - h - y) - k_1(c)h - k_2(c)h + \tilde{k}_i^+ a \\
&\triangleq g_p(a,h,y,c),
\end{aligned} \tag{A35}$$

which where f_p and g_p are used in eqs. (12), (13).

The solution of eq. (A27) separately is

$$y(t) = Ae^{-(C^+ + C^-)t} + \frac{C^+}{C^+ + C^-}. \tag{A36}$$

It follows that the equilibrium solution for the system is

$$y_{eq} = \frac{C^+}{C^+ + C^-} = \frac{(b_3 c + b_1 d_2)(c + d_4)}{(a_1 d_4 + a_3 c)(c + d_2)p + (b_1 d_2 + b_3 c)(c + d_4)} \xrightarrow{p \gg 1} \frac{const}{p}, \tag{A37}$$

in the case of IP$_3$ saturation, we consider $p = [\text{IP}_3]$ to be high. Taking that into account and assuming that waiting time is long enough $t \gg 1/(C^+ + C^-)$ we obtain $y \to 0$. Considering all the assumptions made before, we further operate with the three-variable system taking into account the summing fractions to unity $a + h + z = 1$.

Using the assumption of high [IP$_3$] from (A34), (A35), (A27) we obtain the model illustrated in Fig. 1 (d) and given by eqs. (1), (2).

Appendix B: Stochastic model

In this appendix, we introduce the Langevin model of Ca^{2+} release from a single cluster of channels. By introducing the noise terms into the model from eqs. (1), (2) we obtain

$$da = f(a, h, c)\, dt + As_a\, dW, \tag{B1}$$

$$dh = g(a, h, c)\, dt + As_h\, dW, \tag{B2}$$

where dW are Wiener increments (generated by the Wiener process also known as Brownian motion [53]), s_a and s_h are the functions of the system state in the general case of multiplicative noise, but here for simplicity, we consider $s_a = s_h = 1$ which corresponds to the additive noise case, $A = 0.37$ is the amplitude of the noise.

We integrate the system (B1), (B2) under $c = c_d$ assumption using the Euler-Maruyama method [54] with parameters given in the last column of Tab. I and $N = 7$. The results

presented in Fig. 10 are obtained by analyzing the intervals between 622 puffs using $[Ca^{2+}]$ traces of several thousands of seconds.

---

[1] M. J. Berridge, Biochem Soc T **40**, 297 (2012).

[2] K. Mikoshiba, Biochem Soc Symp **74**, 9 (2007).

[3] Taufiq-Ur-Rahman, A. Skupin, M. Falcke, and C. W. Taylor, Nature **458**, 655 (2009).

[4] I. F. Smith, D. Swaminathan, G. D. Dickinson, and I. Parker, Biophys J **107**, 834 (2014).

[5] G. D. Dickinson, D. Swaminathan, and I. Parker, Biophys J **102**, 1826 (2012).

[6] M. J. Berridge, Biochem Soc Symp **74**, 1 (2007).

[7] G. W. De Young and J. Keizer, P Natl A Sci USA **89**, 9895 (1992).

[8] Y.-X. Li and J. Rinzel, J Theor Biol **166**, 461 (1994).

[9] A. Politi, L. D. Gaspers, A. P. Thomas, and T. Höfer, Biophys J **90**, 3120 (2006).

[10] E. Smedler and P. Uhlén, BBA-Gen Subjects **1840**, 964 (2014).

[11] M. Falcke, Biophys J **84**, 42 (2003).

[12] A. Skupin, H. Kettenmann, U. Winkler, M. Wartenberg, H. Sauer, S. C. Tovey, C. W. Taylor, and M. Falcke, Biophys J **94**, 2404 (2008).

[13] K. Thurley, I. F. Smith, S. C. Tovey, C. W. Taylor, I. Parker, and M. Falcke, Biophys J **101**, 2638 (2011).

[14] R. Kupferman, P. P. Mitra, P. C. Hohenberg, and S. S.-H. Wang, Biophys J **72**, 2430 (1997).

[15] A. Atri, J. Amundson, D. Clapham, and J. Sneyd, Biophys J **65**, 1727 (1993).

[16] J. Sneyd, P. D. Dale, and A. Duffy, SIAM J Appl Math **58**, 1178 (1998).

[17] G. Dupont and A. Goldbeter, Biophys J **67**, 2191 (1994).

[18] A. Calabrese, D. Fraiman, D. Zysman, and S. Ponce Dawson, Phys Rev E **82**, 031910 (2010).

[19] J. Keizer and G. D. Smith, Biophys Chem **72**, 87 (1998).

[20] J. Sneyd and J. Sherratt, SIAM J Appl Math **57**, 73 (1997).

[21] S. P. Dawson, J. Keizer, and J. E. Pearson, P Natl A Sci USA **96**, 6060 (1999).

[22] S. Coombes and Y. Timofeeva, Phys Rev E **68**, 021915 (2003).

[23] S. Rüdiger, Phys Rev E **89**, 062717 (2014).

[24] M. Rückl, I. Parker, J. S. Marchant, C. Nagaiah, F. W. Johenning, and S. Rüdiger, PLOS Comput Biol **11**, e1003965 (2015).

[25] M. Rückl and S. Rüdiger, Eur Phys J E **39**, 1 (2016).

[26] C. W. Taylor and V. Konieczny, Sci Signal **9**, 2 (2016).

[27] Z. Qu, M. B. Liu, and M. Nivala, Sci Rep **6**, 35625 (2016).

[28] J. R. Groff and G. D. Smith, Biophys J **95**, 135 (2008).

[29] R. Hinch, Biophys J **86**, 1293 (2004).

[30] S. M. Wiltgen, G. D. Dickinson, D. Swaminathan, and I. Parker, Cell Calcium **56**, 157 (2014).

[31] D. R. Laver, C. H. T. Kong, M. S. Imtiaz, and M. B. Cannell, J Mol Cell Cardiol **54**, 98 (2013).

[32] S. Rüdiger, P. Jung, and J.-W. Shuai, PLOS Comput Biol **8**, e1002485 (2012).

[33] I. Bezprozvanny, J. Watras, and B. E. Ehrlich, Nature **351**, 751 (1991).

[34] S. Rüdiger, J. W. Shuai, and I. M. Sokolov, Phys Rev Lett **105**, 048103 (2010).

[35] J. Shuai, J. E. Pearson, and I. Parker, Biophys J **95**, 3738 (2008).

[36] A. Dhooge, W. Govaerts, Y. A. Kuznetsov, H. G. Meijer, and Sautois. B., Math Comp Model Dyn **14**, 147 (2008).

[37] Y. A. Kuznetsov, *Elements of Applied Bifurcation Theory*, edited by J. E. Madsen and L. Sirovich (Springer, 2000) pp. 91–112.

[38] N. Callamaras, J. S. Marchant, X.-P. Sun, and I. Parker, J Physiol **509**, 81 (1998).

[39] N. Allbritton, T. Meyer, and L. Stryer, Science **258**, 1812 (1992).

[40] S. Rüdiger, Phys Rep **534**, 39 (2014).

[41] G. D. Dickinson, K. L. Ellefsen, S. P. Dawson, J. E. Pearson, and I. Parker, Sci Signal **9**, ra108 (2016).

[42] J. Marchant, N. Callamaras, and I. Parker, EMBO J **18**, 5285 (1999).

[43] R. FitzHugh, Biophys J **1**, 445 (1961).

[44] C. K. R. T. Jones, T Am Math Soc **286**, 431 (1984).

[45] L. F. Lopez and S. P. Dawson, Phys Biol **13**, 036006 (2016).

[46] Y. Tojyo, T. Morita, A. Nezu, and A. Tanimura, J Pharmacol Sci **107**, 138 (2008).

[47] I. F. Smith, S. M. Wiltgen, J. Shuai, and I. Parker, Sci Signal **2**, ra77 (2009).

[48] S. O. Marx, J. Gaburjakova, M. Gaburjakova, C. Henrikson, K. Ondrias, and A. R. Marks, Circu Res **88**, 1151 (2001).

[49] G. Ullah, I. Parker, D.-O. D. Mak, and J. E. Pearson, Cell Calcium **52**, 152 (2012).

[50] M. D. Bootman, M. J. Berridge, and P. Lipp, Cell **91**, 367 (1997).

[51] J. S. Marchant and I. Parker, EMBO J **20**, 65 (2001).

[52] I. Parker and Y. Yao, J Physiol **491**, 663 (1996).

[53] B. Øksendal, *Stochastic Differential Equations*, 6th ed., Universitext (Springer Berlin Heidelberg, Berlin, Heidelberg, 2003) pp. 109–112.

[54] A. D. Horchler, "Matlab Toolbox for the Numerical Solution of Stochastic Differential Equations (Version 1.2) [Source code]." (2013).